Snowflake divertor configuration studies in National Spherical Torus Experiment[a]

V. A. Soukhanovskii,[1,b] R. E. Bell,[2] A. Diallo,[2] S. Gerhardt,[2] S. Kaye,[2] E. Kolemen,[2]
B. P. LeBlanc,[2] A. G. McLean,[1] J. E. Menard,[2] S. F. Paul,[2] M. Podesta,[2] R. Raman,[3]
T. D. Rognlien,[1] A. L. Roquemore,[2] D. D. Ryutov,[1] F. Scotti,[2] M. V. Umansky,[1] D. Battaglia,[2]
M. G. Bell,[2] D. A. Gates,[2] R. Kaita,[2] R. Maingi,[4] D. Mueller,[2] and S. A. Sabbagh[5]

[1]*Lawrence Livermore National Laboratory, Livermore, California 94551, USA*
[2]*Princeton Plasma Physics Laboratory, Princeton, New Jersey 08543, USA*
[3]*University of Washington, Seattle, Washington 98195, USA*
[4]*Oak Ridge National Laboratory, Oak Ridge, Tennessee 37831, USA*
[5]*Columbia University, New York, New York 10027, USA*

Experimental results from NSTX indicate that the snowflake divertor (D. Ryutov, Phys. Plasmas **14**, 064502 (2007)) may be a viable solution for outstanding tokamak plasma-material interface issues. Steady-state handling of divertor heat flux and divertor plate erosion remains to be critical issues for ITER and future concept devices based on conventional and spherical tokamak geometry with high power density divertors. Experiments conducted in 4–6 MW NBI-heated H-mode plasmas in NSTX demonstrated that the snowflake divertor is compatible with high-confinement core plasma operation, while being very effective in steady-state divertor heat flux mitigation and impurity reduction. A steady-state snowflake divertor was obtained in recent NSTX experiments for up to 600 ms using three divertor magnetic coils. The high magnetic flux expansion region of the scrape-off layer (SOL) spanning up to 50% of the SOL width λ_q was partially detached in the snowflake divertor. In the detached zone, the heat flux profile flattened and decreased to 0.5–1 MW/m^2 (from 4–7 MW/m^2 in the standard divertor) indicative of radiative heating. An up to 50% increase in divertor, P_{rad} in the snowflake divertor was accompanied by broadening of the intrinsic C III and C IV radiation zones, and a nearly order of magnitude increase in divertor high-n Balmer line emission indicative of volumetric recombination onset. Magnetic reconstructions showed that the x-point connection length, divertor plasma-wetted area and divertor volume, all critical parameters for geometric reduction of deposited heat flux, and increased volumetric divertor losses were significantly increased in the snowflake divertor, as expected from theory. © 2012 American Institute of Physics. [http://dx.doi.org/10.1063/1.4737117]

I. INTRODUCTION

The interface between a high-temperature magnetically confined fusion energy (MFE) plasma and a material surface (wall) surrounding the plasma remains to be an outstanding research issue. Presently, a magnetic X-point divertor is envisioned for the plasma-material interface (PMI) in both prospective MFE reactor devices—tokamaks and stellarators.[1,2] In the X-point divertor, a region of open magnetic field lines (the scrape-off layer (SOL)) that surrounds the confined plasma is magnetically diverted away to a separate divertor chamber. The magnetic configuration enables energy and particles lost from the confined core plasma due to radial transport and magnetohydrodynamic instabilities (e.g., edge localized modes (ELMs)) to be directed to the divertor that acts as the PMI. The steady-state peak heat flux endured by the divertor chamber surface is limited by the present day divertor material and active cooling technology constraints at $q_{pk} \leq 10 - 20$ MW/m^2. At higher heat fluxes, the plasma facing component (PFC) lifetime and structural

integrity are at risk due to increased material erosion rates and thermal stress. Additional divertor functions include maintaining the divertor plasma conditions compatible with high-performance high-confinement (H-mode) core plasma, high-pressure pedestal, as well as pedestal region MHD stability for an acceptable ELM regime, and providing impurity control and hydrogenic fuel pumping capabilities.

In the collisional SOL plasma, heat transport parallel to the field lines is often dominated by classical electron and ion conduction, whereas micro-turbulence and intermittency set the cross-field heat and particle transport.[1–5] A fundamental parameter for SOL heat transport is $\lambda_{q_\parallel}$, the SOL power width determined by cross-field and parallel heat transport balance. The SOL power width defines the heat fraction that flows to the divertor, as recently emphasized by a number of tokamak studies.[6–9] At the divertor strike point (SP), peak heat flux q_{pk} can be approximated by a ratio of the power transported to the SP (numerator below) to the plasma-wetted area A_{wet} (denominator below) (e.g., Ref. 10)

$$q_{pk} \simeq \frac{P_{heat}(1 - F_{rad})F_{out/tot}F_{down/tot}(1 - F_{pfr})\sin\alpha}{2\pi R_{SP}f_{exp}\lambda_{q_\parallel}}, \quad (1)$$

where P_{heat} is the input heating power, F_{rad}, $F_{down/tot}$, $F_{out/tot}$, and F_{pfr} are fractions of power going to radiation, lower divertor, outer divertor, and private flux regions, respectively; α is the divertor plate poloidal tilt angle (a deviation from an orthogonal plate); and R_{SP} is the strike point radius. The poloidal magnetic flux expansion f_{exp}—a measure of SOL flux tube flaring in the divertor—is defined as $f_{exp} = (B_p/B_{tot})_{MP} ((B_p/B_{tot})_{outerSP})^{-1}$, where B_p and B_{tot} are the poloidal and total magnetic field at the flux tube strike point and mid-plane (MP) locations.

The divertor heat and particle flux mitigation solutions developed and tested in large tokamaks include active techniques, e.g., impurity or D_2 seeded radiative divertors, field ergodization and strike point sweeping, and passive techniques, e.g., the number of divertors and divertor geometry.[1–3] These solutions, as illustrated by Eq. (1), aim to reduce the parallel heat flux $q_\parallel$ by volumetric power loss processes or SOL power partitioning between divertors, and reduce the heat flux q_{div} deposited on the PFCs by increasing the plasma-wetted surface area.

The spherical tokamak (ST) is viewed as a candidate concept for future fusion and nuclear science applications.[11,12] Divertor experiments in NSTX, a high-power density large ST ($R = 0.85$ m and $a = 0.65$ m) with graphite PFCs,[13,14] have demonstrated the features of the inherently compact ST divertor. ITER-scale steady-state peak divertor heat fluxes $q_{pk} \leq 15$ MW/m^2 and $q_\parallel \leq 200$ MW/m^2 have been measured in $I_p = 1.0 - 1.2$ MA discharges heated by 6 MW neutral beam injection (NBI).[6] As a result of this and other ST- or NSTX-specific geometry features, e.g., a small in/out SOL power ratio, a small divertor PFC area, an open divertor geometry, and reduced divertor volumetric (radiated power and momentum) losses, a reduced operating space of the conventional heat flux mitigation techniques has been observed.[15–17] For future applications, novel integrated approaches are sought, since the radiative divertor technique alone is limited by the divertor radiated power, which does not scale favorably with higher input power or lower density expected in future MFE devices (e.g., Refs. 18 and 19).

Whereas a number of innovative divertor geometry concepts have been put forward in the past (e.g., Refs. 20–23), two new divertor geometries with attractive heat flux handling properties—a Super-X (Refs. 19 and 24) divertor and a snowflake divertor (SFD)[25]—have received much attention recently.[19,24,25] The SFD configuration[25–28] uses a second-order poloidal field null created by merging, or bringing close to each other, two first-order poloidal field null points (X-points) of a standard two-coil divertor configuration. A poloidal cross-section of the obtained magnetic flux surfaces with a hexagonal null-point has an appearance of a snowflake.

Initial results obtained with the SFD configuration in the TCV and NSTX tokamaks demonstrate that this novel divertor geometry may hold promise for outstanding pedestal, ELM, and PMI issues, as well as can be used as a laboratory for pedestal MHD stability and divertor physics studies in existing tokamaks.[29–34] In the initial NSTX experiments, two divertor coils were used to create and maintain the SFD configurations for periods $50 \leq t \leq 150$ ms, enabling the confirmation of the SFD properties predicted by theory.[25,33,34] In this paper, we discuss new SFD experiments in NSTX that took advantage of improved configuration control and diagnostic capabilities and enabled a comprehensive experimental study of the SFD as well as initial comparisons with edge transport modeling. The paper is organized as follows. Section II describes how the new three-coil SFD configuration was developed, obtained, and controlled on NSTX. In Sec. III, we discuss core, pedestal, and divertor properties of the SFD discharges. Section IV describes predictions of a two-dimensional edge transport code for the standard divertor and the SFD. Implications of the NSTX results for the SFD concept are discussed in Sec. V.

II. MAGNETIC PROPERTIES AND CONTROL

In the SFD, the poloidal field B_p increases with distance as r^2 in the vicinity of the second order null (vs r in the vicinity of a first order null in the standard divertor, r being the distance from null), thus leading to (1) a higher poloidal magnetic flux expansion at the divertor (a higher plasma-wetted surface area); (2) a longer X-point connection length L_x; (3) a higher divertor flux tube volume;[26,28] and (4) four separatrix branches and four strike points. In this section, we discuss how these SFD properties were attained in NSTX.

The SFD magnetic equilibria have been simulated for several tokamaks with existing divertor coils.[27] The number of divertor coils needed for the SFD can be as few as two, an attractive feature for future reactors due to engineering and neutron constraints. Whereas an ideal snowflake configuration comprises a second-order null, which is topologically unstable,[26,28] two derivative configurations are of practical interest: a SFD-plus, where the divertor coil currents slightly exceed those of the ideal SFD case, and a SFD-minus, where the corresponding divertor coil currents are slightly lower.[26] Active magnetic control of the SFD configuration is essential in order to maintain and adjust divertor coil currents in real time in response to time-dependent electromagnetic effects.

Modeling of the SFD magnetic configurations with the predictive free-boundary axisymmetric Grad-Shafranov equilibrium code ISOLVER in NSTX suggested that utilization of three existing lower divertor coils may be beneficial for SFD stability. Previously, both the SFD-plus and the SFD-minus configurations were obtained in NSTX with two existing divertor coils operated in a real-time feedback control mode using the plasma control system (PCS) and a strike point control algorithm.[35,36] The scenario used a medium triangularity ($\delta \sim 0.5 - 0.6$) shape maintained by the PCS through an real-time EFIT-based isoflux control algorithm. The new modeling guided the experimental implementation of the three-coil SFD in NSTX. The ISOLVER code used the boundary shape, and the normalized plasma pressure and current profiles from an existing high triangularity discharge (similar to the one shown in Fig. 1(a) to compute the plasma contribution to the flux ψ on a flux surface. Dynamic effects, e.g., the time-dependent plasma inductance, ohmic transformer flux leakage, and variations in divertor structure eddy currents, as well as the plasma edge current, were not
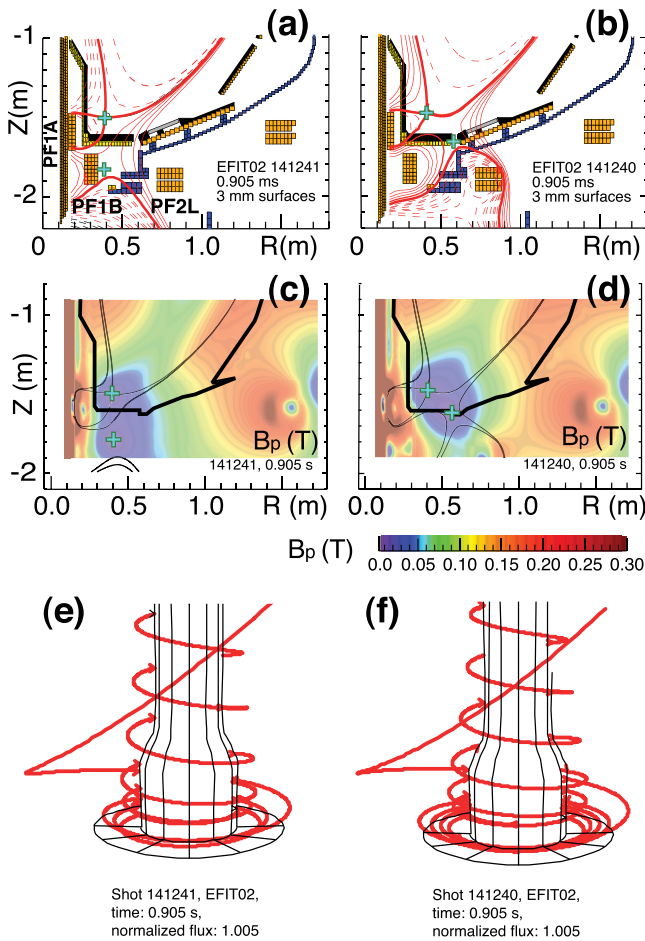
FIG. 1. Poloidal flux contours in the standard (a) and the asymmetric snowflake-minus (b) divertor configurations. Shown are ψ_N separated by 3 mm in the mid-plane. Poloidal magnetic field distribution in the standard (c) and snowflake (d) configurations. Visualization of the field line on the flux surface $\psi_N = 1.005$ in the standard divertor (e) and the snowflake divertor (f).

field lines (B_{tot}) corresponding to the normalized poloidal flux $\psi_N = 1.005$ (approximately $R_\psi - R_{sep} = 1.5$ mm in the mid-plane) are visualized in Figs. 1(e) and 1(f) for the two configurations. The longer magnetic field line length (several more turns in the divertor) in the SFD is clearly visible. Quantitatively, the connection length was by up to a factor of 2 higher in the SFD with respect to the standard divertor configuration. For comparison, the connection length in the lower flux expansion region (e.g., $\psi_N = 1.015$, or approximately 5 mm in the mid-plane) in the SFD was as short as in the standard divertor configuration. A short divertor connection length is a characteristic feature of the standard divertor in the ST.

The new SFD experiments used a well-developed highly shaped standard divertor discharge scenario (e.g., Ref. 37) aiming to integrate the SFD into high-performance long-pulse scenarios.[38] The shaping parameters and wall clearances were controlled with the PCS throughout the entire discharge, while the divertor coil currents used pre-programmed waveforms. Divertor coil current time histories in the SFD discharge are shown in Fig. 2. The SFD discharge scenario used a standard startup, single X-point formation, and the standard divertor configuration before 350 ms. The PF1B and PF2L coil currents were ramped to their nominal SFD values over a transition period that lasted about 200 ms. The asymmetric SFD-minus configuration was established at about 600–650 ms, and lasted for up to 500–600 ms, as evidenced by, e.g., the average X-point flux expansion f_{exp} increase calculated by the EFIT magnetic reconstruction code[39] (Fig. 2(e)).

Because of the dynamic effects mentioned above, operation with pre-programmed divertor coil currents occasionally led to departures from the desired SFD configurations. Fig. 3 illustrates most common SFD failure modes obtained in a
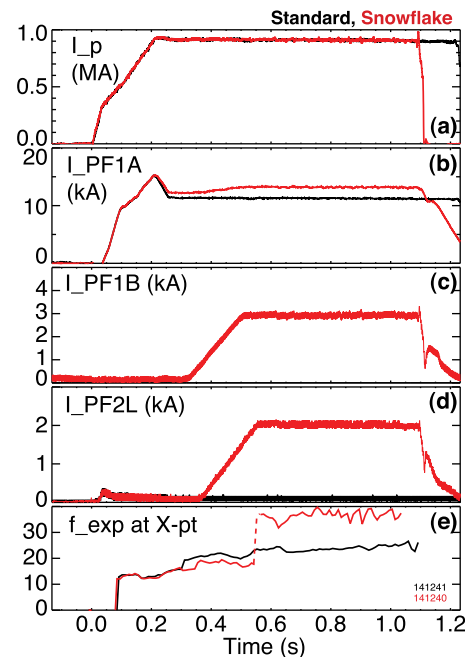
included in the ISOLVER model. Referring to Fig. 1(a), three existing divertor coils PF1A, PF1B, and PF2L with realistic coil currents in the kA range were used to design SFD-minus configurations. The key to the magnetic configuration stability of the three-coil SFD was the use of the middle coil PF1B in reversed polarity with respect to the coils PF1A and PF2L, resulting in a region of opposite magnetic flux in reference to the flux created by the other two divertor coils. This flux region "wedged" between the two nulls and stabilized their relative motion.

The SFD magnetic properties predicted theoretically[25] have been realized in the three-coil SFD in NSTX. Shown in Figs. 1(a) and 1(b) are the poloidal magnetic flux maps of the typical standard divertor and the asymmetric SFD-minus configurations obtained in the experiment. Figs. 1(a) and 1(b) illustrate that the divertor flux expansion was significantly increased. Considering the 3-mm flux tube adjacent to the separatrix, its expansion was up to a factor of 4 higher in the SFD with respect to the standard divertor. The poloidal magnetic field strength is shown in Figs. 1(c) and 1(d). The SFD configuration had a larger region with low $B_p \leq 0.04$ T; it extended over most of the outer and inner divertor legs as well as penetrated deeper into the pedestal region. Magnetic

FIG. 2. Time histories of (a) plasma current I_p; divertor coil currents (b) PF1A; (c) PF1B; (d) PF2L; and (e) X-point flux expansion in the standard divertor (black lines) discharge and the SFD (red lines) discharge.
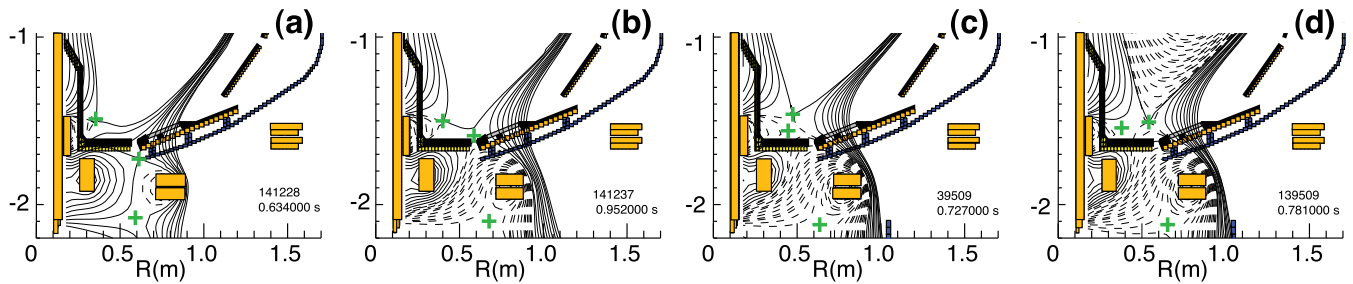
FIG. 3. Examples of SFD-minus configuration failure modes on NSTX. (a) Poloidal field nulls too far; (b) poloidal field null positions too close to divertor plate leading to separatrix touching the PFC; (c) null orientation distorted leading to poloidal flux reconnection and a transient SFD-plus; (d) further motion of secondary null inward from (c) leading to an additional SOL line reconnection and a formation of the SFD-minus in the inner leg.

number of SFD development discharges where divertor coil currents were adjusted to obtain a stable SFD scenario. If I_{PF1B} and I_{PF2L} were too low, the SFD-minus was never realized; instead a high-triangularity standard divertor configuration with a secondary X-point lingering in the SOL periphery was obtained (Fig. 3(a)). If the I_{PF2L} was too high, the SFD-minus became too asymmetric and the secondary X-point brought the separatrix in contact with divertor PFCs (Fig. 3(b)). Having I_{PF1A} too high resulted in an unstable SFD-minus configuration that quickly transitioned to the SFD-plus (Fig. 3(c)) and then often to the asymmetric SFD-minus with the secondary X-point on the inner side with respect to the primary X-point (Fig. 3(d)).

Active magnetic control of the SFD configuration is essential in order to maintain the SFD, e.g., the desired orientation and distance between divertor null-points. Recent analytic developments on the SFD configuration parameterization[40] demonstrate that the described variations of the SFD configuration, i.e., the most commonly encountered asymmetric SFD-minus and SFD-plus configurations (e.g., Fig. 3), can be described mathematically using just one parameter. This can be combined with new developments in the plasma control system.[35,36] A fast numerical algorithm for finding and real-time tracking of the null-point positions will be implemented in NSTX-U.[41]

III. PROPERTIES OF SNOWFLAKE DIVERTOR DISCHARGES

The attainment of steady-state SFD configurations in NSTX has enabled a more detailed study of the core and edge plasma properties. The SFD was found to be compatible with high core and pedestal confinement and stability, while in the divertor, a significant heat flux reduction, increase of impurity radiation, and a radiative detachment of the outer strike zone were observed. These SFD properties are documented and discussed in this section.

The SFD studies in NSTX were carried out in highly shaped ($\kappa \sim 1.9 - 2.0$ and $\delta \sim 0.6 - 0.7$) discharges with $I_p = 0.9$ MA, $B_t = 0.4$ T, and 4–6 MW of NBI heating. Lithium coatings evaporated on PFCs in the amount of 80–100 mg per discharge were used for wall conditioning.[42] In this section, two H-mode discharges with the standard divertor and the SFD (same as in Sec. II) are compared. Core and edge diagnostics used in this study have been described elsewhere (Refs. 17 and references therein).

A. Core and pedestal

The SFD was found to be compatible with high confinement plasma operation, with no degradation in H-mode core performance. Highly radiative and detached divertor operation is a concern for core plasma performance as high divertor n_e and low T_e can lead to an X-point MARFE formation, degrade the pedestal pressure (by lowering pedestal T_e), and lead to a significant confinement degradation. Shown in Figs. 4(a)–4(d) are the time traces of core plasma parameters ($\bar{n}_e$, central T_e, β_N, and W_{MHD}) in the two discharges. Similar high performance metrics of these discharges, e.g., $\tau_E \simeq 50 - 60$ ms, $W_{MHD} \simeq 200 - 250$ kJ, and the factor H98(y,2)$\simeq 1$ calculated using the TRANSP code, suggested that the snowflake phase did not have any degrading effect on the core plasma.

The snowflake divertor phase had a profound effect on plasma impurity content. The ELM-free H-mode standard divertor discharges obtained in NSTX with lithium conditioning had impurity accumulation leading to high average plasma charge $Z_{eff} \leq 3 - 4$ due to carbon and high core radiated power $P_{rad} \leq 1 - 3$ MW due to metallic impurities.[43,44] In the initial NSTX snowflake divertor experiment, significant reductions in core carbon density (concentration), as
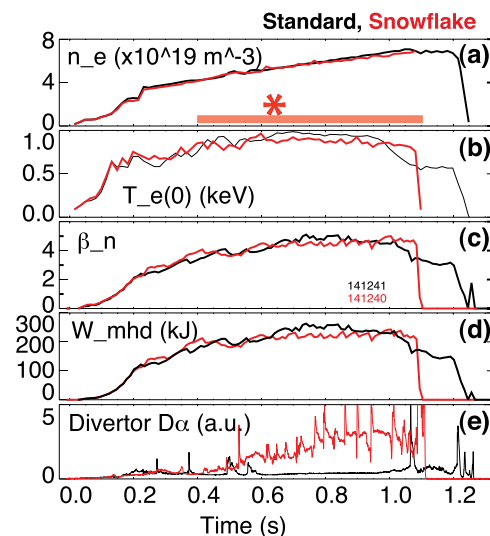

FIG. 4. Time histories of core and edge plasma quantities in the standard divertor (black traces) and the SFD (red): (a) Averaged density n_e; (b) Central electron temperature T_e; (c) Normalized β_N; (d) Core plasma stored energy W_{tot}; and (e) Lower divertor total D_α intensity.
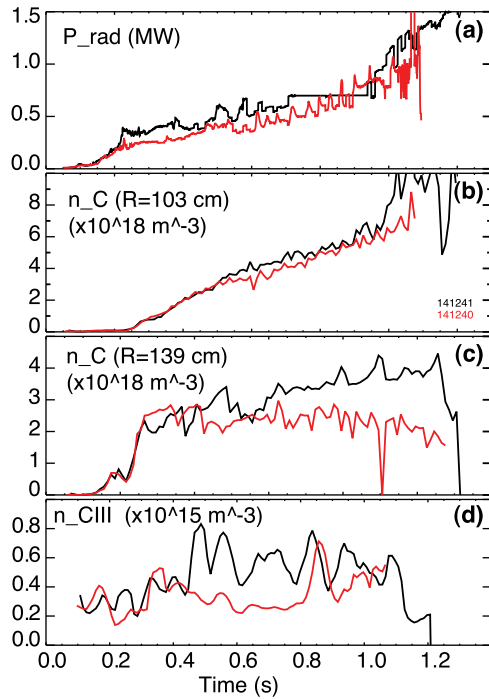
FIG. 5. Time histories of core and edge impurity quantities in the standard divertor (black traces) and the SFD (red): (a) Total plasma P_{rad}; (b) Central carbon density n_C; (c) Pedestal carbon density n_C; and (d) Near-separatrix C III density.

well as radiated power were noted. In the discussed discharges, the core plasma radiated power P_{rad} was reduced by 10%-20% in the SFD discharge. Large reductions in n_C and n_C/n_e were measured in all SFD discharges, as illustrated in Figs. 5 and 6. The reduction was pronounced in the pedestal region ($R \sim 139$ cm), where carbon tended to accumulate. The total carbon inventory N_c was reduced by 50%–70%. The observed reduction of carbon in the SFD discharges could be attributed to a number of factors: modifications to the edge radial impurity transport, modifications to the SOL force balance that changed parallel carbon transport, as well as the reduction of physical and chemical sputtering fluxes in the detached SFD, and at the wall. Some impurity reduction may also be attributed to the particle expulsion effect of large Type I ELMs that appeared in the SFD phase. While a full analysis of these carbon transport and source mechanisms is planned and will be reported elsewhere, some preliminary comments can be made. The steady-state between-ELM carbon profiles shown in Fig. 6 appear to differ from the standard divertor discharge only by a scaling factor, with insignificant differences in $T_i(R)$ and $n_i(R)$. We also note that both the standard divertor and the SFD discharges did not have low toroidal wavenumber (n) tearing mode activity that was often present in NSTX discharges and that could change macroscopic details of impurity profiles. MHD spectrograms based on the Mirnov coil measurements showed the presence of $n=1$ (and sometimes $n=2,3$) modes early
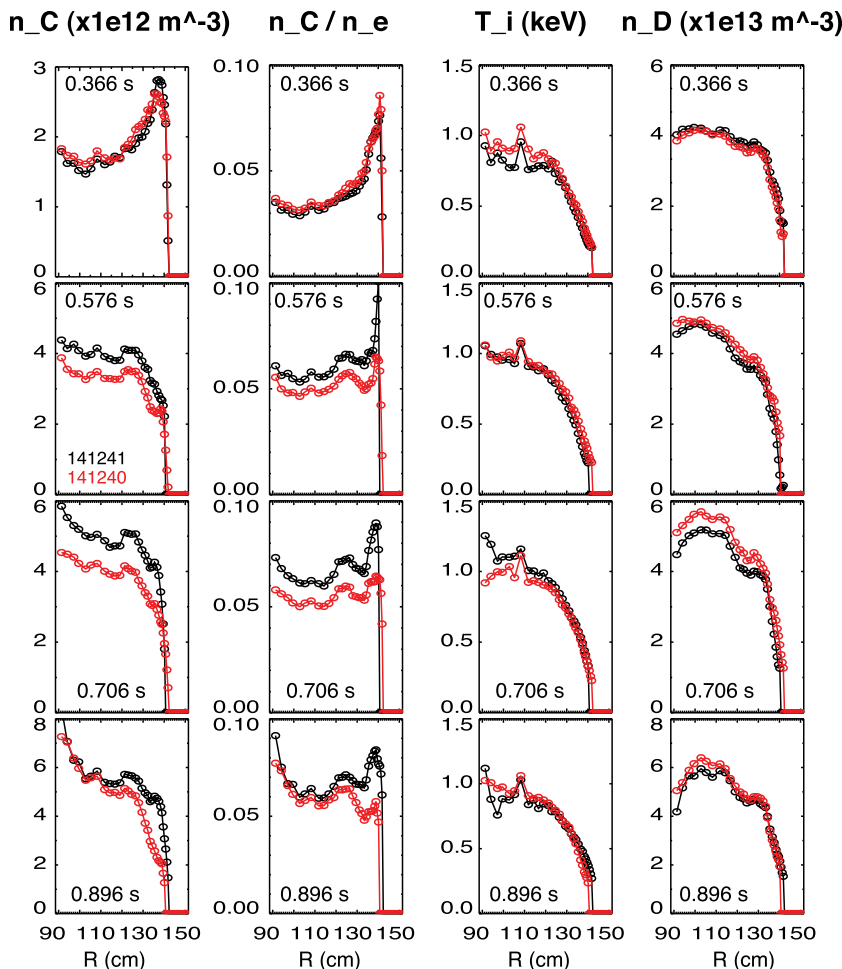

FIG. 6. Time evolution of plasma profiles, carbon density ($n_C(R)$, first column), carbon concentration ($n_C(R)/n_e(R)$ second column), carbon ion temperature ($T_i(R)$, third column), and deuterium ion density ($n_D(R)$, forth column), in the standard divertor discharge (black traces) and the SFD discharge (red) at the four times before and during the SFD formation, as discussed in Sec. III B.

($t \leq 0.5$ s) and late ($t \geq 0.95 - 1.0$ s) in the discharges but not during the comparison period. Impurity transport in NSTX H-mode discharges has been previously found to be close to neoclassical in the core region $\rho \leq 0.8 - 0.9$,[45,46] being in the Pfirsch-Schluter regime and driven by ∇T_i and ∇n_i. The similarity of the $n_C(R)$, $n_D(R)$, and $T_i(R)$ profiles may suggest similar impurity transport in both discharges with a reduced edge carbon source in the SFD. The edge C III density, estimated from C III brightness measurements, $T_e(r)$, $n_e(r)$ and the Atomic Data and Analysis Structure (ADAS) photon emission coefficients (as was done in Ref. 15), differed by up to 50% between the standard divertor and the snowflake phase (Fig. 5(d)), further suggesting that the edge carbon source was reduced.

Theoretical analysis of a SFD configuration showed that an increased magnetic shear inside the separatrix in the SFD configuration can lead to stronger stabilization of ideal MHD modes.[26,47] While the analysis of the pedestal MHD stability in the NSTX SFD discharges is deferred to a separate publication, we note that the SFD formation resulted in modifications to edge stability and led to re-appearance of large type I ELMs with $\Delta W_{tot}/W_{tot} \sim 5\% - 12\%$. In the standard divertor discharge, ELMs were suppressed by means of lithium wall conditioning.[48] As was proposed in Ref. 49, lithium coatings on lower divertor PFCs modified edge pressure and current profiles and led to low-n peeling-ballooning mode stabilization. We also note that the enhanced stability of the peeling-ballooning modes in the pedestal region (and generally an extended second stability region), as well as an H-mode pedestal regime with reduced type I ELM frequency and slightly increased normalized ELM energy were observed in the SFD experiments on the TCV tokamak, where the SFD was obtained in steady-state by means of six divertor coils.[29–32]

B. Scrape-off layer and divertor

As in the initial SFD experiment in NSTX that used two divertor coils, a significant reduction of divertor heat flux and increase in divertor carbon radiation was observed in the three-coil SFD. The SFD formation was always followed by a partial detachment of the outer strike point. In spite of the detachment, high core confinement was maintained for many τ_E, up to 500–600 ms. In this section, divertor measurements are compared between the standard divertor and the SFD, using either the two previously discussed discharges (standard divertor vs SFD), or the SFD discharge alone, where the standard divertor phase is compared to the SFD phase. The emphasis in this analysis is given to the dynamics of previously unavailable steady-state measurements of outer divertor heat flux and radiation profiles. The inner divertor strike point was on the vertical target (inner wall) in both the standard divertor and the SFD; however, its conditions could not be fully characterized because of poor diagnostic coverage of the vertical target region.

A significant heat flux reduction concomitant with the SFD formation was evident in the two-color infrared camera measurements of divertor surface temperature. Total divertor heat flux (in the electron and ion channels) was inferred from the calibrated surface IR thermography[50,51] using the THEODOR code[52] which had a one-dimensional PFC heat conduction model and a surface layer parameter $\alpha = 10\,000$. Shown in Fig. 7 are the contour plots of divertor heat fluxes for the standard divertor and the SFD discharges. In the standard divertor discharge, the outer strike point position drifted outward. The outer strike point region (with some fine structure likely induced by error fields) was clearly observable. The standard divertor was characterized by $f_{exp} \sim 20$, SOL power width $\lambda_q \sim 6 - 8$ mm, and $q_{\parallel}^{outerSP} = 40 - 100$ MW/m^2. The SFD discharge started in the standard divertor configuration with high heat flux $q_{peak} \leq 7$ MW/m^2 ($q_{\parallel} \leq 130$ MW/m^2). The SFD formation during the time period 0.50–0.70 s was clearly seen in the heat flux data: the heat load footprint was split between the outer strike point region and the low-flux expansion region at $R = 0.55 - 0.65$ m as the secondary X-point approached the divertor floor (i.e., the configurations shown in Figs. 1(a) and 1(b)). In the high flux expansion region, the heat flux profile narrowed and q_{peak} decreased to $q_{peak} \leq 2$ MW/m^2 at the onset of detachment around 0.7 s.

The heat flux reduction was a result of the SFD geometry and the $q_{\parallel}$ reduction due to volumetric power and momentum loss processes: impurity radiation, charge exchange, and recombination. Shown in Fig. 8 are the time traces comparing divertor measurements in the standard divertor and the SFD discharges. Both discharges had $P_{SOL} \sim 3$ MW. The outer target in the standard divertor configuration received $Q_{div} = 1.8 - 2.0$ MW, as shown in Fig. 8(a). The quantity Q_{div} was obtained by a spatial integration of the heat flux profiles from the IR thermography. During the SFD formation phase, the divertor heat flux decreased to about
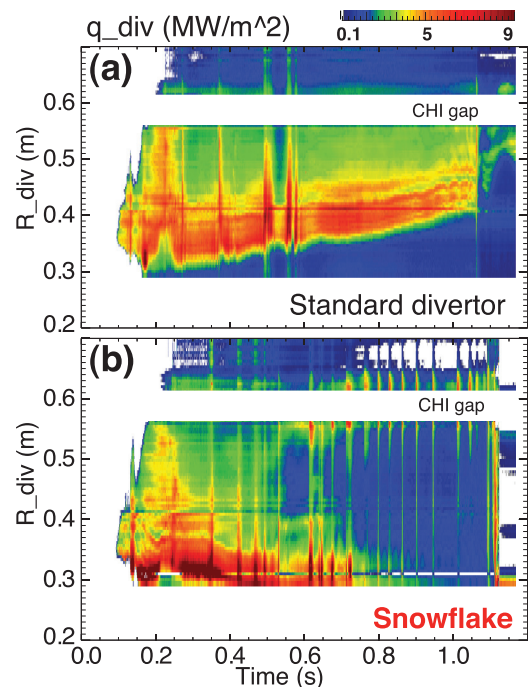

FIG. 7. Contour plots of divertor heat flux as a function of time and divertor R in the standard divertor (a) and SFD (b). CHI gap is a physical gap between divertor target plates where infrared thermography measurements cannot be performed.
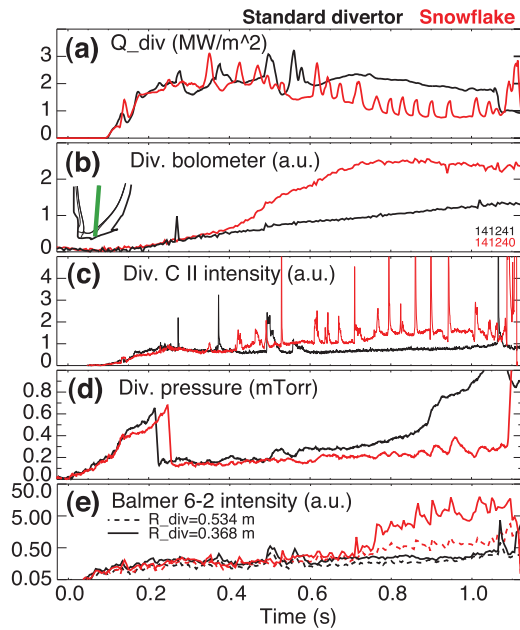
FIG. 8. Time histories of divertor quantities in the standard divertor (black traces) and the SFD (red) discharges: (a) divertor heating power Q_{div}; (b) divertor bolometer vertical chord signal (viewing geometry shown in inset); (c) divertor C II intensity; (d) divertor pressure; (e) Balmer $n = 6$-2 line intensity in the strike point region $R_{div} = 0.368$ m and in the periphery of the high flux expansion zone $R_{div} = 0.534$ m.

$Q_{div} = 1.0 - 1.2$ MW. The peak heat flux was gradually reduced during the SFD formation from 4–$7\,\text{MW/m}^2$ to about 2–$3\,\text{MW/m}^2$. Divertor radiated power P_{rad}, as illustrated in Fig. 8 by one vertical bolometer chord signal and divertor C II emission intensity, gradually increased. Divertor neutral pressure measured by a Penning gauge[53] under the divertor plate remained similar in both configurations (Figs. 8(d)). This was somewhat surprising in view of the clear signs of strike point detachment onset. If the divertor brightness increase of the Balmer $n = 6$–2 line is taken as an indication of the volumetric recombination onset accompanying the detachment (as in previous radiative divertor experiments[15,17,33]), the onset of the partial strike point detachment occurred about 700 ms. Shown in Fig. 8(e) are two spectroscopic views, one viewing through the X-point region and

the strike point region and another viewing through the 2–3 mm flux surface; both indicated a substantial increase in divertor recombination rate throughout half of the SOL width. After the partial detachment onset, the peak heat flux decreased further down to 0.5–$1\,\text{MW/m}^2$, while the total power Q_{div} received by the outer divertor decreased to below 1 MW.

In order to separate the effect of the radiative detachment from the SFD geometric effects, we consider divertor heat fluxes and radiation profiles at four times evaluated between ELMs in the SFD discharge: (1) before the SFD is formed (standard divertor with $f_{exp} \sim 20$) at $t = 0.360$ s; (2) and (3)—during the SFD formation—0.57 and 0.70 s, the latter point just prior to the detachment onset; and (4)—at 0.895 s in the radiative detachment phase. Quantitative power balance analysis was not possible, since full bolometric divertor coverage was not available. However, spectroscopic measurements of D I, Li I, Li II and C II, CIII, C IV visible emission could be used to elucidate on the P_{rad} distribution in the divertor region.

True-color visible camera images of entire NSTX plasmas showed the continuous increase of divertor radiation with the SFD formation. Shown in Figs. 9(a)–9(d) are the full plasma images of the standard divertor discharge. The orange-red color is representative of the bright D$_\alpha$ line at 656.1 nm and Li I lines at 610.8 and 670.5 nm. Green and blue color emissions are dominated by Li II and C II, C III lines. Strong radiation was observed in the lower divertor strike point regions, while weak radiation was observed in the upper divertor region and the inner wall gas injection port (visible as a bright gas cloud in the middle of the center stack). Insidentally, the camera frame shown in Fig. 9(b) captured a MARFE (a green emission ring around the center stack) that often occurred in the standard divertor discharges.[54] The SFD images shown in Figs. 9(e)–9(h) clearly demonstrate an increase in radiation and its spatial extent in the lower divertor region in the SFD formation phase and a greater increase in the SFD radiative detachment phase. The visible emission in the lower divertor was dominated by the bright D$_\alpha$ line. Interestingly, in the upper divertor, the color of emission changed from red-orange in the standard divertor phase to blue-green in the snowflake phase (Figs. 9(e)–9(h))
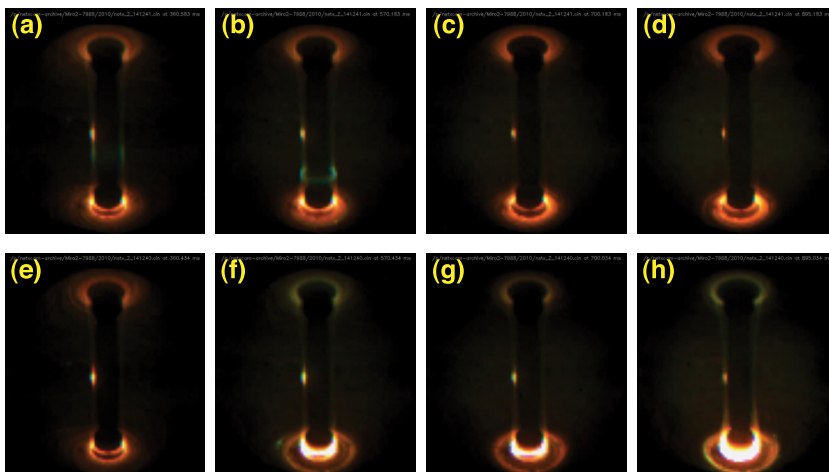
FIG. 9. Visible color camera images of entire NSTX plasmas: top panels—the standard divertor discharge (a)–(d), bottom panels (e)–(h)—the SFD discharge. Images are representative of the times discussed in the text: 0.360 s—(a) and (e); 0.570 s—(b) and (f); 0.700 s—(c) and (g); and 0.895 s—(d) and (h).
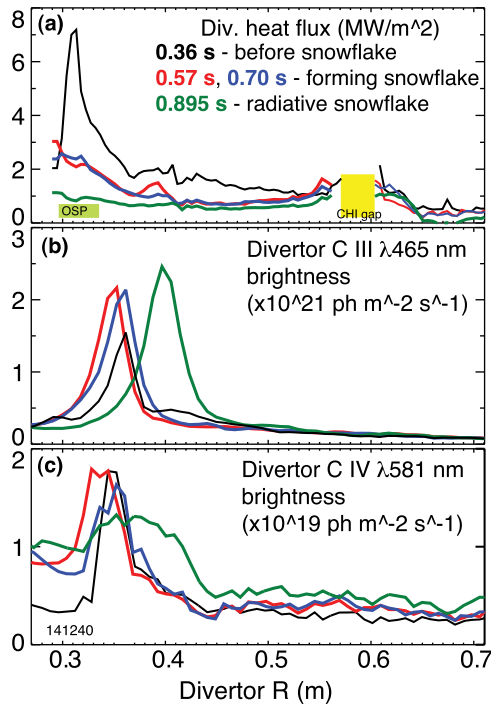
FIG. 10. Divertor profiles at different times of the SFD discharge (a) heat flux; (b) C III brightness; and (c) C IV brightness.

possibly indicating a higher T_e or a stronger interaction with graphite PFCs.

A large fraction of SOL heat flux in the SFD divertor appeared to be radiated by carbon impurities. Shown in Fig. 10 are the lower divertor heat flux, C III and C IV brightness profiles at the times of interest in the SFD discharge: at 0.36 s, 0.57 s, 0.70 s, and at 0.895 s. During the SFD formation the heat flux profile, albeit reduced peak values, showed some peaking in the separatrix region ($R = 0.30 - 0.35$ m). The profile became nearly flat in the radiatively detached snowflake phase, suggesting predominantly radiative surface heating. Parallel heat flux can be inferred from the heat flux profiles $q_\perp(R_{div})$ as $q_\parallel = q_\perp/\sin(\gamma))$, where γ is the angle between the total magnetic field line and the divertor PFC surface. In the outer strike point region, before the SFD formation $q_\parallel = 100 - 115$ MW/m^2, while in the SFD formation phase, $q_\parallel = 30 - 80$ MW/m^2. This reduction is thought to be a result of increased heat flux diffusion into the private

flux region because of a longer L_x, as well as increased radiated power loss because of a higher divertor volume and a lower divertor T_e, as suggested by impurity radiation time traces. After the onset of radiative detachment, the P_{rad} fraction increases further, bringing the parallel heat flux down and also apparently heating the surface. This is confirmed by carbon radiation profiles measured by divertor viewing cameras, as shown in Figs. 10(b) and 10(c). The C III and C IV brightness profiles showed a significant broadening and increase in peak radiation during the SFD formation. The CII time trace (Fig. 2) also showed an additional increase at about 0.70 ms. As carbon radiation is maximized at $T_e \leq 10$ eV, the increase in carbon emission suggested that with the SFD formation, the divertor plasma became cooler and denser.

An important limitation of high flux expansion divertors is the shallow angle between total magnetic field lines and the divertor PFC surface. This suggests the criticality for the PFC alignment, as misaligned PFC tile leading edges can be overheated, melted, or eroded at a faster rate. The magnetic field line angle $\sim 1° - 2°$ is considered compatible with the present engineering constraints on the divertor PFC element alignment.[55] In the NSTX SFD experiments, the angle γ in the SFD outer strike point region was $0.5° - 2°$. Temperature measurements of the lower divertor graphite tile surface, performed by the two-dimensional IR thermography in the SFD discharges, indicated that tile misalignment was not a concern at 4 MW NBI heating. Shown in Fig. 11 are the divertor plate temperature distributions from IR thermography, and the calculated angles γ with respect to the horizontal divertor target, for the four times of interest before, during and after the formation of the SFD. As the standard divertor configuration evolved into the SFD configuration, the divertor surface temperature, including the SP region, decreased from $500° - 1000°$C to $200° - 400°$C, and no enhanced heating of tile edges was observed. Because of the $q_\parallel$ reduction due to impurity radiation, the SFD operation did not have any adverse impact on PFC tiles.

IV. EDGE TRANSPORT MODEL DEVELOPMENT

To obtain a better understanding of divertor heat transport, power balance and radiation distribution in the SFD, as well as to enable projections to higher power density
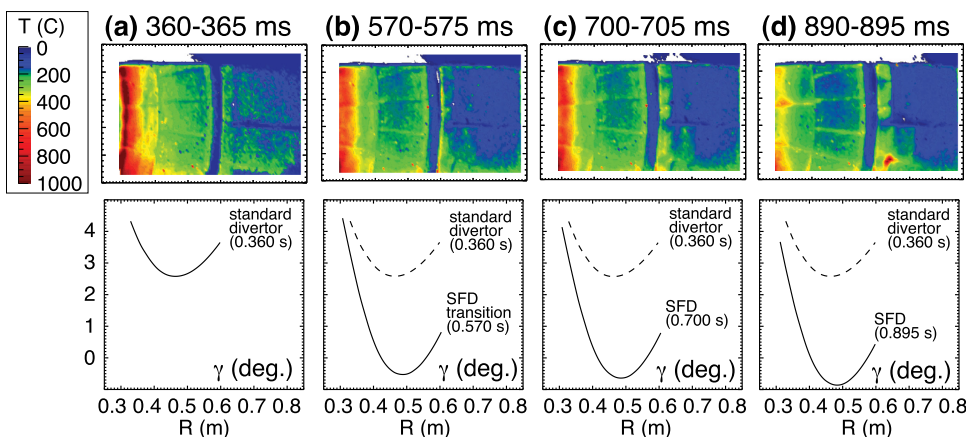

FIG. 11. Lower divertor surface temperature (upper panels) and magnetic field incidence angle γ (bottom panels) in the SFD discharge at the times (a) before the SFD formation—0.360 s; forming SFD—(b) 0.570 s and (c) 0.700 s; and (d) radiative SFD—0.895 s. The dashed line in the bottom panels shows the standard divertor angle γ at $t = 0.360$ s from (a) for comparison.
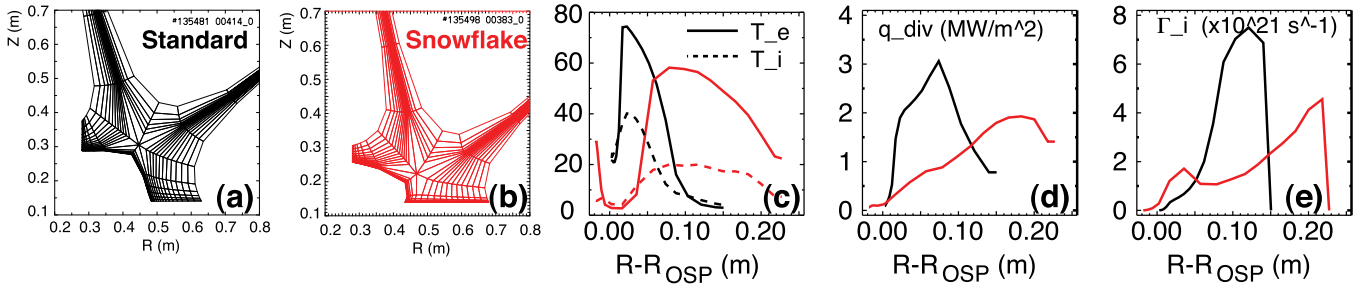
FIG. 12. Initial UEDGE model results of the standard divertor (black lines) and SFD (red lines): (a) and (b) divertor region computation mesh; divertor plate profiles: (c) T_e, T_i, (d) heat flux q_{div}; and (e) particle flux Γ_i.

devices, a two-dimensional transport model of the NSTX SFD experiment is developed. In this section, we discuss the methodology of the model development and initial modeling results of the NSTX SFD obtained with the UEDGE code.

Previously, edge plasma transport modeling confirmed the SFD geometry benefits for divertor heat load mitigation. Two-dimensional multi-fluid transport models based on the UEDGE code[56] have been created for a number of simulated SFD configurations.[27,28,47] The models demonstrated that (1) the heat flux in the SFD was reduced with respect to the standard divertor and the reduction was stronger than just the ratio of the plasma-wetted areas; it also included the reduction due to increased volumetric losses; (2) the detachment threshold expressed in terms of the edge n_e was lower in the SF divertor in comparison with the standard divertor. Both modeling conclusions are in qualitative agreement with the NSTX SFD experiment and motivate the NSTX SFD model development.

The model development for NSTX started with an accurate two-dimensional numerical mesh that was based on the MHD equilibrium from the experiment.[33,34] Conventional MHD equilibria calculated on a 64×64 mesh lacked the spatial resolution in the divertor null-point region, so higher resolution equilibria with resolutions up to 121×121 were used. The curvilinear meshes were generated for the standard divertor and for the snowflake-minus configurations. The divertor region meshes are shown in Figs. 12(a) and 12(b). The cells extend to the divertor plates (which are not shown) and the mesh spans the radial region $\psi_N = 0.95 - 1.04$ in normalized flux coordinates. The presence of the secondary poloidal field null in the divertor region is generally a concern for mesh generation codes. However, for these asymmetric SFD equilibria, the secondary null point was always outside of the mesh domain (under the divertor surface in the physical domain). Revisions to the modified numerical mesh generation algorithm implemented in UEDGE (Ref. 57) may be necessary if a mesh for an arbitrary two-null geometry (as, e.g., in Figs. 3(b)–3(d)) is desirable.

The UEDGE code solves the Braginskii transport equations for plasma particles, momentum, and energy[56] and reduced Navier-Stokes equations for neutral transport. Core boundary conditions for the NSTX model were defined by $P_{SOL} \simeq 3$ MW equally divided over the electron and ion channels and the particle flux Γ_i. Radial transport was modeled by *adhoc* convection and diffusion coefficients $\chi_{e,i} = 0.5$ m^2/s and $D = 0.25$ m^2/s that were selected on the basis of

previously developed NSTX UEDGE models.[58,59] In the initial transport simulations, nominal NSTX parameters were used. A core-plasma interface at $\psi_N = 0.95$ was assumed having $T_e = 120$ eV, $T_i = 120$ eV, and $n_e = 4.5 \times 10^{19}$ m^2 (not yet representative of the experiment). A fixed impurity fraction model with a carbon concentration of 3% and the PFC recycling coefficient 0.95 were used. The initial model, nonetheless, showed many differences between the standard divertor and the SFD cases in a qualitative agreement with the experiment. Shown in Figs. 12(c)–12(e) is a comparison of the modeled divertor profiles. The divertor T_e, T_i were reduced in the high flux expansion zone of the outer divertor leg, as were the heat and particle fluxes to the divertor plate. The simulations indicated a tendency for a colder, denser plasma in the SFD vs. the standard divertor, however, did not yet indicate the radiative detachment observed in the experiment. The tendency observed in this initial model was representative of the transition phase between the standard divertor and the SFD discussed in Sec. III B. A further development of the model will include additional adjustments to the radial transport coefficients and boundary conditions (primarily the PFC recycling coefficient and the impurity model) to enable a closer match to the experimental upstream profiles and divertor power and particle measurements, as has been done for a number of standard divertor UEDGE simulations.[60–62] Once plausible models of the standard divertor and the SFD are obtained, they can be used to study the impact of external parameters, e.g., higher input power, impurities (including additional impurity seeding) and cryopumping, as well as geometric factors, on the SFD conditions.

V. DISCUSSION

Results presented in this paper demonstrate significant benefits in the SFD configuration, namely, divertor heat flux reduction via increased plasma-wetted area and volumetric losses, and edge stability modifications, in agreement with theory predictions. This work also highlighted the areas for future SFD studies: real-time feedback control of magnetic configuration, impurity production and transport, edge pedestal MHD stability and ELM regimes, the role of divertor radiation, and compatibility of the SFD with divertor pumping. In this section, we discuss some of these issues further.

Real-time feedback control of the SFD configuration remains to be one of the critical issues that has not been

tested in the experiment. While conceptually the control of the two null-point and strike point positions is possible,[35,36] the algorithm needs to be implemented in the PCS and tested with real power supplies and with electromagnetically induced time-varying and transient currents. The reported SFD results were obtained in the configuration classified as an asymmetric snowflake-minus,[40] where the secondary null lies close to (or at) the separatrix on the outer SOL side. Transient snowflake-plus (with the secondary null point in the private flux region) and ideal snowflake configurations have also been obtained on NSTX with two and three divertor coils. From the control side, the asymmetric snowflake-minus might be easier to maintain, as the snowflake-plus and the ideal snowflake appeared to be more susceptible to poloidal magnetic flux variations leading to the loss of these configurations.

More experimental work is needed to clarify the divertor power balance and the separation of heat flux reduction effects due to the geometry and volumetric losses. The issue is important for future discharge scenarios involving the SFD, e.g., in the event when the SFD configuration is lost due to plasma motion, or the partial detachment may not be possible due to low SOL collisionality. In NSTX SFD discharges, the radiative detachment was always obtained at or shortly after the SFD formation. Present work leads us to conclude that during the transition phase to the SFD, divertor dissipative losses were increased continuously until the partial detachment occurred. The attached SFD (during the formation phase) reduced steady-state heat flux by 50%-60% and increased divertor P_{rad} by up to 50%. The partial detachment brought additional dissipative losses. This results was characteristic of the experiment with $P_{SOL} = 3$ MW and the divertor geometry (e.g., particular L_x, f_{exp}, etc); however, an extension to higher SOL power is needed to understand how the detachment is linked to the SFD effects. Higher power experiments would also clarify the scaling of heat flux in the low flux expansion zone of the divertor, where volumetric losses are apparently not as large and where sheath-limited SOL heat transport is expected.

Present SFD results can be projected onto the divertor heat flux operating space in NSTX.[6,63] In previous NSTX divertor experiments, q_{pk} showed a linear scaling with P_{SOL} and a weak dependence on n_e.[6,63] Partial detachment of the outer strike point was previously obtained in NSTX standard divertor discharges using either extrinsic D_2 or CD_4 puffing,[15,17] or in configurations with a low X-point height.[16] In standard divertor configurations with SOL power $1.5 \leq P_{SOL} \leq 5$ MW, the outer strike point detachment did not occur without gas seeding because of insufficient divertor carbon P_{rad} in the compact NSTX divertor. The SFD magnetic properties affected parallel divertor heat transport in the near-SOL region by increasing both collisionality and the volumetric losses (via the divertor volume). This resulted in a partial detachment of the outer strike point, despite the counterbalancing effect of lithium conditioning that tended to reduce recycling and the divertor n_e. As a result, divertor power density was reduced to 0.5–1 MW/m^2 at $P_{SOL} \sim 3$ MW. A similar reduction was obtained with extrinsic D_2 injection in the standard divertor configuration.

One of the core plasma observations with the SFD includes a significant core impurity reduction. However, further work is also needed to elucidate on the impurity sputtering sources and SOL parallel transport in SFD discharges. Shallow magnetic field line angles in the divertor could lead to significant plasma-surface interaction effects, e.g.: modifications of the sheath structure and potential, leading to reduced ion energy E_i, reduced secondary electron emission, ultimately leading to reduced impurity sputtering.[64–69] In NSTX experiments, evaporated lithium coatings on graphite PFCs were used, thus both carbon and lithium must be considered in a full impurity sputtering and divertor radiation analysis. In a divertor strike point region with $T_e \leq 1 - 5$ eV, a significant reduction of divertor carbon physical sputtering rates as well as an improved impurity entrainment in a hydrogenic plasma flow are expected.[17,70–72] The role of lithium coatings on carbon sputtering as well as on divertor radiation should also be clarified. The lithium radiated power cooling curve peaks at $T_e \sim 1$ eV under coronal conditions and can extend the peak to higher T_e under the influence of non-coronal effects. Enhanced plasma interaction with the vaporized lithium region could also be expected at shallow magnetic field line angles.

Experimental results from NSTX, as well as from TCV tokamak, motivate further snowflake experiment and theory developments aimed at the PMI for future high-power density devices. In particular, the NSTX Upgrade[41] will require a significant PMI development to handle the projected steady-state 20–40 MW/m^2 peak divertor heat fluxes[6] in 2 MA discharges up to 5 s long with up to 12 MW NBI heating. Future plans for the NSTX Upgrade include two up-down symmetric sets of four divertor coils for developing upper and lower divertor snowflake configurations. These configurations are being developed using the predictive free boundary Grad-Shafranov code ISOLVER, and initial results are very encouraging.

VI. CONCLUSIONS

Experimental results from NSTX indicate that the snowflake divertor may be a viable solution for the outstanding tokamak PMI issues. Experiments conducted in 4–6 MW NBI-heated H-mode plasmas demonstrate that the SFD is compatible with high-confinement core plasma operation, while being very effective in steady-state divertor heat flux mitigation and impurity reduction. Magnetic reconstructions show that the critical divertor parameters, such as X-point connection length, divertor plasma-wetted area, and divertor volume, are all modified in the SFD in a favorable way, as expected from theory. While the present experiments demonstrated the achievement of these parameters for many core energy confinement times, i.e., essentially in steady-state, one of the remaining issues is the magnetic control of the steady-state SFD configuration. Future research on NSTX Upgrade and other facilities will focus on details of the heat transport and power balance in the SFD, the SFD operation with active pumping (e.g., Ref. 73), the pedestal stability and ELMs, and the magnetic control of the SFD. Plasma discharge scenarios having

lower and upper SFD are being developed to address the needs of future ST-based devices.

ACKNOWLEDGMENTS

[1]ITER Physics Expert Group on Divertor, ITER Physics Expert Group on Divertor Modelling, and Database and ITER Physics Basis Editors, Nucl. Fusion **39**, 2391 (1999).

[2]A. Loarte, B. Lipschultz, A. Kukushkin, G. Matthews, P. Stangeby, N. Asakura, G. Counsell, G. Federici, A. Kallenbach, K. Krieger, A. Mahdavi, V. Philipps, D. Reiter, J. Roth, J. Strachan, D. Whyte, R. Doerner, T. Eich, W. Fundamenski, A. Herrmann, M. Fenstermacher, P. Ghendrih, M. Groth, A. Kirschner, S. Konoshima, B. LaBombard, P. Lang, A. Leonard, P. Monier-Garbet, R. Neu, H. Pacher, B. Pegourie, R. Pitts, S. Takamura, J. Terry, E. Tsitrone, the ITPA Scrape-off Layer, and D. P. T. Group, Nucl. Fusion **47**, S203 (2007).

[3]B. Lipschultz, X. Bonnin, G. Counsell, A. Kallenbach, A. Kukushkin, K. Krieger, A. Leonard, A. Loarte, R. Neu, R. Pitts, T. Rognlien, J. Roth, C. Skinner, J. Terry, E. Tsitrone, D. Whyte, S. Zweben, N. Asakura, D. Coster, R. Doerner, R. Dux, G. Federici, M. Fenstermacher, W. Fundamenski, P. Ghendrih, A. Herrmann, J. Hu, S. Krasheninnikov, G. Kirnev, A. Kreter, V. Kurnaev, B. Labombard, S. Lisgo, T. Nakano, N. Ohno, H. Pacher, J. Paley, Y. Pan, G. Pautasso, V. Philipps, V. Rohde, D. Rudakov, P. Stangeby, S. Takamura, T. Tanabe, Y. Yang, and S. Zhu, Nucl. Fusion **47**, 1189 (2007).

[4]A. Leonard, M. A. Mahdavi, S. L. Allen, N. H. Brooks, M. E. Fenstermacher, D. N. Hill, C. J. Lasnier, R. Maingi, G. D. Porter, T. W. Petrie, J. G. Watkins, and W. P. West, Phys. Rev. Lett. **78**, 4769 (1997).

[5]C. Hidalgo, B. Gonçalves, C. Silva, M. A. Pedrosa, K. Erents, M. Hron, and G. F. Matthews, Phys. Rev. Lett. **91**, 065001 (2003).

[6]T. Gray, R. Maingi, V. Soukhanovskii, J. Surany, J.-W. Ahn, and A. McLean, J. Nucl. Mater. **415**, S360 (2011).

[7]B. LaBombard, J. Terry, J. Hughes, D. Brunner, J. Payne, M. Reinke, I. Cziegler, R. Granetz, M. Greenwald, I. Hutchinson, J. Irby, Y. Lin, B. Lipschultz, Y. Ma, E. Marmar, W. Rowan, N. Tsujii, G. Wallace, D. Whyte, S. Wolfe, S. Wukitch, and G. Wurden, Phys. Plasmas **18**, 056104 (2011).

[8]T. Eich, B. Sieglin, A. Scarabosio, W. Fundamenski, R. Goldston, and A. Herrmann, Phys. Rev. Lett. **107**, 215001 (2011).

[9]C. J. Lasnier, M. A. Makowski, J. A. Boedo, S. L. Allen, N. H. Brooks, D. N. Hill, A. W. Leonard, J. G. Watkins, and W. P. West, J. Nucl. Mater. **415**, S353 (2011).

[10]S. Jardin, C. Kessel, T. Mau, R. Miller, F. Najmabadi, V. Chan, M. Chu, R. LaHaye, L. Lao, T. Petrie, P. Politzer, H. StJohn, P. Snyder, G. Staebler, A. Turnbull, and W. West, Fusion Eng. Des. **80**, 25 (2006).

[11]Y.-K. Peng, P. Fogarty, T. Burgess, D. Strickler, B. Nelson, J. Tsai, C. Neumeyer, R. Bell, C. Kessel, J. Menard, D. Gates, B. Leblanc, D. Mikkelsen, E. Fredrickson, L. Grisham, J. Schmidt, P. Rutherford, S. Sabbagh, A. Field, A. Sykes, I. Cook, O. Mitarai, and Y. Takase, Plasma Phys. Controlled Fusion **47**, 263 (2005).

[12]R. Goldston, J. Menard, J. Allain, J. Brooks, J. Canik, R. Doerner, G.-Y. Fu, D. Gates, C. Gentile, J. Harris, A. Hassanein, N. Gorelenkov, R. Kaita, S. Kaye, M. Kotschenreuther, G. Kramer, H. Kugel, R. Maingi, S. Mahajan, R. Majeski, C. Neumeyer, R. Nygren, M. Ono, L. Owen, S. Ramakrishnan, T. Rognlien, D. Ruzic, D. Ryutov, S. Sabbagh, C. Skinner, V. Soukhanovskii, T. Stevenson, M. Ulrickson, P. Valanju, and R. Woolley, "Fusion energy," in *Proc. 22nd Int. Conf. Geneva, 2008*, CD-ROM file FT/P3-12 (IAEA, Vienna, 2008), http://www-naweb.iaea.org/napc/physics/FEC/FEC2008/html/node101.htm#23954.

[13]M. Ono, S. Kaye, Y.-K. Peng, G. Barnes, W. Blanchard, M. Carter, J. Chrzanowski, L. Dudek, R. Ewig, D. Gates, R. Hatcher, T. Jarboe, S. Jardin, D. Johnson, R. Kaita, M. Kalish, C. Kessel, H. Kugel, R. Maingi, R. Majeski, J. Manickam, B. McCormack, J. Menard, D. Mueller, B. Nelson, B. Nelson, C. Neumeyer, G. Oliaro, F. Paoletti, R. Parsells, E. Perry, N. Pomphrey, S. Ramakrishnan, R. Raman, G. Rewoldt, J. Robinson, A. Roquemore, P. Ryan, S. Sabbagh, D. Swain, E. Synakowski, M. Viola, M. Williams, J. Wilson, and N. Team, Nucl. Fusion **40**, 557 (2000).

[14]R. Raman, J.-W. Ahn, J. Allain, R. Andre, R. Bastasz, D. Battaglia, P. Beiersdorfer, M. Bell, R. Bell, E. Belova, J. Berkery, R. Betti, J. Bialek, T. Bigelow, M. Bitter, J. Boedo, P. Bonoli, A. Boozer, A. Bortolon, D. Brennan, J. Breslau, R. Buttery, J. Canik, G. Caravelli, C. Chang, N. Crocker, D. Darrow, W. Davis, L. Delgado-Aparicio, A. Diallo, S. Ding, D. D'Ippolito, C. Domier, W. Dorland, S. Ethier, T. Evans, M. Finkenthal, J. Foley, R. Fonck, R. Frazin, E. Fredrickson, G. Fu, D. Gates, S. Gerhardt, A. Glasser, N. Gorelenkov, T. Gray, Y. Guo, W. Guttenfelder, T. Hahm, R. Harvey, A. Hassanein, W. Heidbrink, K. Hill, Y. Hirooka, E. Hooper, J. Hosea, B. Hu, D. Humphreys, K. Indireshkumar, F. Jaeger, T. Jarboe, S. Jardin, M. Jaworski, R. Kaita, J. Kallman, O. Katsuro-Hopkins, S. Kaye, C. Kessel, J. Kim, E. Kolemen, S. Krasheninnikov, S. Kubota, H. Kugel, R. La Haye, L. Lao, B. LeBlanc, W. Lee, K. Lee, J. Leuer, F. Levinton, Y. Liang, D. Liu, J. Luhmann, N., R. Maingi, R. Majeski, J. Manickam, D. Mansfield, R. Maqueda, E. Mazzucato, A. McLean, D. McCune, B. McGeehan, G. McKee, S. Medley, J. Menard, M. Menon, H. Meyer, D. Mikkelsen, G. Miloshevsky, D. Mueller, T. Munsat, J. Myra, B. Nelson, N. Nishino, R. Nygren, M. Ono, T. Osborne, H. Park, J. Park, S. Paul, W. Peebles, B. Penaflor, C. Phillips, A. Pigarov, M. Podesta, J. Preinhaelter, Y. Ren, H. Reimerdes, G. Rewoldt, P. Ross, C. Rowley, E. Ruskov, D. Russell, D. Ruzic, P. Ryan, S. Sabbagh, M. Schaffer, E. Schuster, F. Scotti, K. Shaing, V. Shevchenko, K. Shinohara, V. Sizyuk, C. Skinner, A. Smirnov, D. Smith, P. Snyder, W. Solomon, A. Sontag, V. Soukhanovskii, T. Stoltzfus-Dueck, D. Stotler, B. Stratton, D. Stutman, H. Takahashi, Y. Takase, N. Tamura, X. Tang, C. Taylor, G. Taylor, C. Taylor, K. Tritz, D. Tsarouhas, M. Umansky, J. Urban, M. Walker, W. Wampler, W. Wang, J. Whaley, R. White, J. Wilgen, R. Wilson, K. Wong, J. Wright, Z. Xia, D. Youchison, G. Yu, H. Yuh, L. Zakharov, D. Zemlyanov, G. Zimmer, and S. Zweben, Nucl. Fusion **51**, 094011 (2011).

[15]V. Soukhanovskii, R. Maingi, D. Gates, J. Menard, S. Paul, R. Raman, A. Roquemore, M. Bell, R. Bell, J. Boedo, C. Bush, R. Kaita, H. Kugel, B. LeBlanc, and D. Mueller, Phys. Plasmas **16**, 022501 (2009).

[16]V. A. Soukhanovskii, R. Maingi, R. E. Bell, D. A. Gates, R. Kaita, H. W. Kugel, B. P. LeBlanc, R. Maqueda, J. E. Menard, D. Mueller, S. F. Paul, R. Raman, and A. L. Roquemore, "High flux expansion divertor studies in NSTX," in 36th EPS Conference on Plasma Physics, Sofia, Bulgaria, 2009, http://arxiv.org/abs/0912.4281.

[17]V. Soukhanovskii, R. Maingi, D. Gates, J. Menard, S. Paul, R. Raman, A. Roquemore, R. Bell, C. Bush, R. Kaita, H. Kugel, B. LeBlanc, and D. Mueller, Nucl. Fusion **49**, 095025 (2009).

[18]J. Canik, R. Maingi, L. Owen, J. Menard, R. Goldston, M. Kotschenreuther, P. Valanju, and S. Mahajan, J. Nucl. Mater. **390–391**, 315 (2009).

[19]M. Kotschenreuther, P. Valanju, S. Mahajan, and J. Wiley, Phys. Plasmas **14**, 72502 (2007).

[20]C. Kahn, K. Burrell, S. Ejima, E. Fairbanks, T. Petrie, M. Ssimada, and M. Washizu, Nucl. Fusion **26**, 73 (1986).

[21]M. Mahdavi, S. Allen, M. Fenstermacher, R. Maingi, M. Schaffer, R. Stambaugh, and M. Wade, Fusion Sci. Technol. **48**, 1072 (2005).

[22]H. Takase, J. Phys. Soc. Jpn. **70**, 609 (2001).

[23]J. Kesner, Nucl. Fusion **30**, 548 (1990).

[24]P. Valanju, M. Kotschenreuther, S. Mahajan, and J. Canik, Phys. Plasmas **16**, 056110 (2009).

[25]D. Ryutov, Phys. Plasmas **14**, 064502 (2007).

[26]D. Ryutov, R. Cohen, T. Rognlien, and M. Umansky, Phys. Plasmas **15**, 092501 (2008).

[27]D. Ryutov, R. Bulmer, R. Cohen, D. Hill, L. Lao, J. Menard, T. Petrie, L. Pearlstein, T. Rognlien, P. Snyder, V. Soukhanovskii, and M. Umansky, "Fusion energy," in *Proc. 22nd Int. Conf. Geneva, 2008*, CD-ROM file IC/P4-8 (IAEA, Vienna, 2008), http://www-naweb.iaea.org/napc/physics/FEC/FEC2008/html/node199.htm#43720.

[28]M. Umansky, R. Bulmer, R. Cohen, T. Rognlien, and D. Ryutov, Nucl. Fusion **49**, 075005 (2009).

[29]F. Piras, S. Coda, I. Furno, J.-M. Moret, R. Pitts, O. Sauter, B. Tal, G. Turri, A. Bencze, B. Duval, F. Felici, A. Pochelon, and C. Zucca, Plasma Phys. Controlled Fusion **51**, 055009 (2009).

[30]F. Piras, S. Coda, B. Duval, B. Labit, J. Marki, S. Medvedev, J.-M. Moret, A. Pitzschke, and O. Sauter, Plasma Phys. Controlled Fusion **52**, 124010 (2010).

[31]F. Piras, S. Coda, B. Duval, B. Labit, J. Marki, S. Medvedev, J.-M. Moret, A. Pitzschke, and O. Sauter, Phys. Rev. Lett. **105**, 155003 (2010).

[32]S. Medvedev, A. Ivanov, A. Martynov, Y. Poshekhonov, R. Behn, Y. Martin, J.-M. Moret, F. Piras, A. Pitzschke, A. Pochelon, O. Sauter, and L. Villard, Contrib. Plasma Phys. **50**, 324 (2010).

[33]V. Soukhanovskii, J. Ahn, R. Bell, D. Gates, S. Gerhardt, R. Kaita, E. Kolemen, H. Kugel, B. LeBlanc, R. Maingi, R. Maqueda, A. McLean, J. Menard, D. Mueller, S. Paul, R. Raman, A. Roquemore, D. Ryutov, and H. Scott, J. Nucl. Mater. **415**, S365 (2011).

[34]V. Soukhanovskii, J.-W. Ahn, R. Bell, D. Gates, S. Gerhardt, R. Kaita, E. Kolemen, B. LeBlanc, R. Maingi, M. Makowski, R. Maqueda, A. McLean, J. Menard, D. Mueller, S. Paul, R. Raman, A. Roquemore, D. Ryutov, S. Sabbagh, and H. Scott, Nucl. Fusion **51**, 012001 (2011).

[35]E. Kolemen, D. Gates, C. Rowley, N. Kasdin, J. Kallman, S. Gerhardt, V. Soukhanovskii, and D. Mueller, Nucl. Fusion **50**, 105010 (2010).

[36]E. Kolemen, D. Gates, S. Gerhardt, R. Kaita, H. Kugel, D. Mueller, C. Rowley, and V. Soukhanovskii, Nucl. Fusion **51**, 113024 (2011).

[37]D. Gates, R. Maingi, J. Menard, S. Kaye, S. Sabbagh, G. Taylor, J. Wilson, M. Bell, R. Bell, S. Bernabei, J. Bialek, T. Biewer, W. Blanchard, J. Boedo, C. Bush, M. Carter, W. Choe, N. Crocker, D. Darrow, W. Davis, L. Delgado-Aparicio, S. Diem, J. Ferron, A. Field, J. Foley, E. Fredrickson, R. Harvey, R. Hatcher, W. Heidbrink, K. Hill, J. Hosea, T. Jarboe, D. Johnson, R. Kaita, C. Kessel, S. Kubota, H. Kugel, J. Lawson, B. LeBlanc, K. Lee, F. Levinton, J. Manickam, R. Maqueda, R. Marsala, D. Mastrovito, T. Mau, S. Medley, H. Meyer, D. Mikkelsen, D. Mueller, T. Munsat, B. Nelson, C. Neumeyer, N. Nishino, M. Ono, H. Park, W. Park, S. Paul, W. Peebles, M. Peng, C. Phillips, A. Pigarov, R. Pinsker, A. Ram, S. Ramakrishnan, R. Raman, D. Rasmussen, M. Redi, M. Rensink, G. Rewoldt, J. Robinson, P. Roney, L. Roquemore, E. Ruskov, P. Ryan, H. Schneider, C. Skinner, D. Smith, A. Sontag, V. Soukhanovskii, T. Stevenson, D. Stotler, B. Stratton, D. Stutman, D. Swain, E. Synakowski, Y. Takase, K. Tritz, A. Von Halle, M. Wade, R. White, J. Wilgen, M. Williams, W. Zhu, S. Zweben, R. Akers, P. Beiersdorfer, R. Betti, and T. Bigelow, Phys. Plasmas **13**, 056122 (2006).

[38]S. Gerhardt, D. Gates, S. Kaye, R. Maingi, J. Menard, S. Sabbagh, V. Soukhanovskii, M. Bell, R. Bell, J. Canik, E. Fredrickson, R. Kaita, E. Kolemen, H. Kugel, B. Le Blanc, D. Mastrovito, D. Mueller, and H. Yuh, Nucl. Fusion **51**, 073031 (2011).

[39]S. Sabbagh, S. Kaye, J. Menard, F. Paoletti, M. Bell, R. Bell, J. Bialek, M. Bitter, E. Fredrickson, D. Gates, A. Glasser, H. Kugel, L. Lao, B. LeBlanc, R. Maingi, R. Maqueda, E. Mazzucato, D. Mueller, M. Ono, S. Paul, M. Peng, C. Skinner, D. Stutman, G. Wurden, W. Zhu, and N. R. Team, Nucl. Fusion **41**, 1601 (2001).

[40]D. Ryutov, M. Makowski, and M. Umansky, Plasma Phys. Controlled Fusion **52**, 105001 (2010).

[41]J. E. Menard, S. Gerhardt, M. Bell, J. Bialek, A. Brooks, J. Canik, J. Chrzanowski, M. Denault, L. Dudek, D. A. Gates, N. Gorelenkov, W. Guttenfelder, R. Hatcher, J. Hosea, R. Kaita, S. Kaye, C. Kessel, E. Kolemen, H. Kugel, R. Maingi, M. Mardenfeld, D. Mueller, B. Nelson, C. Neumeyer, M. Ono, E. Perry, R. Ramakrishnan, R. Raman, Y. Ren, S. Sabbagh, M. Smith, V. Soukhanovskii, T. Stevenson, R. Strykowsky, D. Stutman, G. Taylor, P. Titus, K. Tresemer, K. Tritz, M. Viola, M. Williams, R. Woolley, H. Yuh, H. Zhang, Y. Zhai, A. Zolfaghari and the NSTX Team, Nucl. Fusion **52**, 083015 (2012).

[42]H. W. Kugel, M. G. Bell, J. W. Ahn, J. P. Allain, R. Bell, J. Boedo, C. Bush, D. Gates, T. Gray, S. Kaye, R. Kaita, B. LeBlanc, R. Maingi, R. Majeski, D. Mansfield, J. Menard, D. Mueller, M. Ono, S. Paul, R. Raman, A. L. Roquemore, P. W. Ross, S. Sabbagh, H. Schneider, C. H. Skinner, V. Soukhanovskii, T. Stevenson, J. Timberlake, W. R. Wampler, and L. Zakharov, Phys. Plasmas **15**, 056118 (2008).

[43]S. Paul, C. Skinner, J. Robinson, B. LeBlanc, and H. Kugel, J. Nucl. Mater. **390–391**, 211 (2009).

[44]J. M. Canik, R. Maingi, T. E. Evans, R. E. Bell, S. P. Gerhardt, B. P. LeBlanc, J. Manickam, J. E. Menard, T. H. Osborne, J.-K. Park, S. F. Paul, P. B. Snyder, S. A. Sabbagh, H. W. Kugel, and E. A. Unterberg, Phys. Rev. Lett. **104**, 045001 (2010).

[45]L. Delgado-Aparicio, D. Stutman, K. Tritz, F. Volpe, K. L. Wong, R. Bell, M. Finkenthal, E. Fredrickson, S. P. Gerhardt, S. Kaye, B. LeBlanc, J. Menard, S. Paul, and L. Roquemore, Nucl. Fusion **51**, 083047 (2011).

[46]L. Delgado-Aparicio, D. Stutman, K. Tritz, M. Finkenthal, S. Kaye, R. Bell, R. Kaita, B. LeBlanc, F. Levinton, J. Menard, S. Paul, D. Smith, and H. Yuh, Nucl. Fusion **49**, 085028 (2009).

[47]M. Umansky, T. Rognlien, D. Ryutov, and P. Snyder, Contrib. Plasma Phys. **50**, 350 (2010).

[48]D. Mansfield, H. Kugel, R. Maingi, M. Bell, R. Bell, R. Kaita, J. Kallman, S. Kaye, B. LeBlanc, D. Mueller, S. Paul, R. Raman, L. Roquemore, S. Sabbagh, H. Schneider, C. Skinner, V. Soukhanovskii, J. Timberlake, J. Wilgen, and L. Zakharov, J. Nucl. Mater. **390–391**, 764 (2009).

[49]R. Maingi, T. H. Osborne, B. P. LeBlanc, R. E. Bell, J. Manickam, P. B. Snyder, J. E. Menard, D. K. Mansfield, H. W. Kugel, R. Kaita, S. P. Gerhardt, S. A. Sabbagh, and F. A. Kelly, Phys. Rev. Lett. **103**, 075001 (2009).

[50]J.-W. Ahn, R. Maingi, D. Mastrovito, and A. Roquemore, Rev. Sci. Instrum. **81**, 023501 (2010).

[51]A. McLean, J.-W. Ahn, R. Maingi, T. Gray, and L. Roquemore, Rev. Sci. Instrum. (submitted).

[52]A. Herrmann, W. Junker, K. Gunther, S. Bosch, M. Kaufmann, J. Neuhauser, G. Pautasso, T. Richter, and R. Schneider, Plasma Phys. Controlled Fusion **37**, 17 (1995).

[53]R. Raman, H. W. Kugel, R. Gernhardt, T. Provost, T. R. Jarboe, and V. Soukhanovskii, Rev. Sci. Instrum. **75**, 4347 (2004).

[54]R. Maqueda, R. Maingi, K. Tritz, K. Lee, C. Bush, E. Fredrickson, J. Menard, A. Roquemore, S. Sabbagh, and S. Zweben, J. Nucl. Mater. **363–365**, 1000 (2007).

[55]A. Herrmann, Plasma Phys. Controlled Fusion **44**, 883 (2002).

[56]T. D. Rognlien, J. L. Milovich, M. E. Rensink, and G. D. Porter, J. Nucl. Mater. **196–198**, 347 (1992).

[57]M. Petravic, J. Comput. Phys. **73**, 125 (1987).

[58]M. E. Rensink, H. W. Kugel, R. Maingi, F. Paoletti, G. D. Porter, T. D. Ronglien, S. Sabbagh, and X. Xu, J. Nucl. Mater. **290–293**, 706 (2001).

[59]V. A. Soukhanovskii, R. Maingi, A. L. Roquemore, J. Boedo, C. Bush, R. Kaita, H. W. Kugel, B. P. Leblanc, S. F. Paul, G. D. Porter, and N. S. Wolf, J. Nucl. Mater. **337–339**, 475 (2005).

[60]N. S. Wolf, G. D. Porter, D. N. Hill, and S. L. Allen, J. Nucl. Mater. **266–269**, 739 (1999).

[61]G. D. Porter, R. Isler, J. Boedo, and T. D. Rognlien, Phys. Plasmas **7**, 3663 (2000).

[62]G. D. Porter, T. W. Petrie, T. D. Rognlien, and M. E. Rensink, Phys. Plasmas **17**, 112501 (2010).

[63]R. Maingi, C. Bush, R. Kaita, H. Kugel, A. Roquemore, S. Paul, and V. Soukhanovskii, J. Nucl. Mater. **363–365**, 196 (2007).

[64]C. H. Wu, J. Nucl. Mater. **160**, 103 (1988).

[65]A. Futch, G. Matthews, D. Buchenauer, D. Hill, R. Jong, and G. Porter, J. Nucl. Mater. **196–198**, 860 (1992).

[66]T. Q. Hua and J. N. Brooks, Phys. Plasmas **1**, 3607 (1994).

[67]Y. Igitkhanov and G. Janeschitz, J. Nucl. Mater. **290–293**, 99 (2001).

[68]S. Takamura, M. Y. Ye, T. Kuwabara, and N. Ohno, Phys. Plasmas **5**, 2151 (1998).

[69]D. D. Ryutov, Contrib. Plasma Phys. **2**, 207 (1996).

[70]D. Whyte, W. West, C. Wong, R. Bastasz, J. Brooks, W. Wampler, N. Brooks, J. Davis, R. Doerner, A. Haasz, R. Isler, G. Jackson, R. Macaulay-Newcombe, and M. Wade, Nucl. Fusion **41**, 1243 (2001).

[71]O. Gruber, A. Kallenbach, M. Kaufmann, K. Lackner, V. Mertens, J. Neuhauser, F. Ryter, H. Zohm, M. Bessenrodt-Weberpals, K. Büchl, S. Fiedler, A. Field, C. Fuchs, C. Garcia-Rosales, G. Haas, A. Herrmann, W. Herrmann, S. Hirsch, W. Köppendörfer, P. Lang, G. Lieder, K.-F. Mast, C. S. Pitcher, M. Schittenhelm, J. Stober, W. Suttrop, and M. Troppmann, Phys. Rev. Lett. **74**, 4217 (1995).

[72]H. S. Bosch, R. Dux, G. Haas, A. Kallenbach, M. Kaufmann, K. Lackner, V. Mertens, H.-D. Murmann, W. Poschenrieder, H. Salzmann, J. Schweinzer, W. Suttrop, and M. Weinlich, Phys. Rev. Lett. **76**, 2499 (1996).

[73]V. A. Soukhanovskii, J.-W. Ahn, M. G. Bell, R. E. Bell, D. A. Gates, and S. Gerhardt, "Fusion energy," in *Proc. 23nd Int. Conf. Daejon, 2010*, CD-ROM file EXD/P3-32 (IAEA, Vienna, 2010).